Building and Environment 119 (2017) 44–61

Contents lists available at ScienceDirect

Building and Environment

journal homepage: www.elsevier.com/locate/buildenv

On the use of non-conformal grids for economic LES of wind flow and convective heat transfer for a wall-mounted cube

S. Iousef [a, *], H. Montazeri [b, c], B. Blocken [b, c], P.J.V. van Wesemael [a]

[a] Architectural Urban Design and Engineering, Department of the Built Environment, Eindhoven University of Technology, Eindhoven, The Netherlands
[b] Building Physics Section, Department of Civil Engineering, KU Leuven, Leuven, Belgium
[c] Building Physics and Services, Department of the Built Environment, Eindhoven University of Technology, Eindhoven, The Netherlands

ARTICLE INFO

Article history:
Received 24 November 2016
Received in revised form
4 April 2017
Accepted 5 April 2017
Available online 6 April 2017

Keywords:
Non-conformal grids
Sensitivity analysis
Conjugate heat transfer
Convective heat transfer coefficients
LES

ABSTRACT

Generating economical, high-resolution and high-quality computational grids for Large Eddy Simulation (LES) of wind flow and convective heat transfer (CHT) around surface-mounted obstacles is not straightforward. When the grid size is used as filter, LES grids should ideally consist of cubic cells, while CHT requires a very high near-wall resolution to resolve the thin viscous sublayer and buffer layer that represent the largest resistance to CHT. To avoid very high cell numbers and the need for excessive computational resources, non-conformal grids can be considered. This paper provides a detailed evaluation of the performance of non-conformal grids with cubic cells, for wind flow and CHT around a wall-mounted cubic obstacle. LES results on non-conformal versus conformal grids are compared with each other and with wind-tunnel measurements of wind speed and surface temperature. Moreover, sensitivity analysis is performed concerning the impact of overall grid resolution, subdomain size and grid refinement ratio. Average absolute deviations between LES on non-conformal versus conformal grids are about 0.9% (0.5 °C) for surface temperature on all cube surfaces. Comparison with experiments shows for the non-conformal grid an average and maximum absolute deviation for surface temperature of 2.0% (1.1 °C) and 7.6% (3.6 °C), respectively. The sensitivity analysis shows minor impact of subdomain size on convective heat transfer coefficients (CHTC) where, on average, absolute deviations of less than 2.2% are observed. This study shows that non-conformal grids can strongly reduce the total cell count (here by a factor up to 30.2) without significantly compromising the accuracy of results.

1. Introduction

With the advancement of computational power and numerical methods, the use of Computational Fluid Dynamics (CFD) in wind engineering, also referred to as Computational Wind Engineering, has seen a rapid growth in the past 50 years, covering a wide range of topics encountered within the lower part of the atmospheric boundary layer (ABL) [1–3]. A problem of particular interest in wind engineering, building physics and urban physics is the analysis of convective heat transfer (CHT) across building facades and roofs [4–6]. The knowledge of the so-called convective heat transfer coefficients (CHTC) is important for the assessment of urban heat islands (UHI), building energy demand for heating and cooling, etc.

Accurate analysis of CHT is subject to at least two important requirements. First, it strictly requires resolving the entire boundary layer, including the very thin viscous sublayer and buffer layer that dominate the convective surface resistance. This in turn requires computational grids with a very high near-wall resolution, in the order of 100 μm for building applications, as employed in some recent studies [7,8]. Second, accurate analysis requires transient simulations with Large Eddy Simulation (LES) to capture the complex flow patterns around bluff bodies, like buildings [9–12]. In the framework of implicit filtering in LES, where the grid size is used as filter, ideally, grids should consist of cubic cells as they present equal filter length in all three directions. The combination of these two requirements provides an exceptional challenge in grid generation, certainly for high Reynolds (Re) number flow as encountered in wind engineering, where the overall dimensions of the problem under study can easily be five orders of magnitude larger than the thickness of the viscous sublayer and hence the size of the near-wall cells.

* Corresponding author.
E-mail address: s.iousef@tue.nl (S. Iousef).

http://dx.doi.org/10.1016/j.buildenv.2017.04.004

Regular conformal grids, which present a matching of nodes (with a very low tolerance) at the formed interfaces, would easily yield excessively large total numbers of cells and similarly excessive required computational resources for the assessment of CHTC. In order to combine grid economy with the requirements of high grid resolution and high grid quality for CHT on surfaces of wall-mounted obstacles, non-conformal grids can be considered. In contrast to conformal grids, non-conformal grids form interfaces where at least one of the nodes, on the one side of the interface, is not matched with another node on the other side of the interface.

Non-conformal grids are used as means towards grid economy, which is needed in order for computationally expensive and/or large-scale simulations to be performed. Moreover, the employment of non-conformal grids easily allows providing sufficient resolution in the regions of the flow where this is actually needed. This especially holds when LES is employed, where the effects of the subgrid-scale (SGS) model can be of critical importance [13,14]. However, for SGS models, used for representing the effect of unresolved quantities, the filter width is usually proportional to the grid resolution. As a result, in case of non-conformal grids, a sudden refinement or coarsening of the grid may result in discontinuities in eddy viscosity, which, in turn, can lead to numerical instabilities. Piomelli et al. [15] investigated the effect of non-conformal grids on LES statistics in turbulent plane channel flow with different SGS models. Their study distinguished between two types of non-conformal interfaces: (i) parallel and (ii) normal to the mean advection direction. They observed that an interface parallel to the mean advection did not result in significant discontinuities. However, in case the interface was placed normal to the mean advection, large jumps in the resolved shear stresses, especially close to the wall, were observed. Vanella et al. [16] extended the work by Piomelli et al. [15] and studied a simple case of turbulent flow. Grid coarsening or refinement by a factor of 2 in all directions was considered. The results showed that, in the case of sudden grid refinement, significant perturbations were not observed in the flow, as gradual generation of the small scales and a smooth transition of the flow across the interfaces occured. On the other hand, in the case of grid coarsening, a considerable energy pile-up at small scales was observed near the interfaces. The aforementioned studies [15,16] focused mainly on the analysis of simple flow configurations in plane channel and uniform flows across non-conformal interfaces and did not take into consideration heat transfer.

In the present paper a detailed evaluation of the performance of non-conformal grids, consisting entirely of cubic cells, for wind flow and CHT around a wall-mounted cubic obstacle is provided. First, a comparison of LES results on non-conformal versus conformal grids is performed. The differences between the LES results are quantified and the related reduction in the total cell count and associated computational resources due to the use of a non-conformal grid are reported. Then, a comparison of the LES results with wind-tunnel measurements of wind speed and surface temperature is conducted and the accuracy of the numerical predictions is demonstrated by validation metrics. Finally, a sensitivity analysis is performed concerning the impact of overall grid resolution, subdomain size and grid refinement ratio on the LES results. Recommendations are provided to support future CFD studies of wind flow and CHT around surface-mounted bluff bodies, like buildings, in turbulent boundary layer flow. It is stressed that the intention of this paper is not to conduct an LES simulation of wind flow and CHT that is as accurate as possible. On the contrary, the intention of this paper is to depart as much as possible in terms of cell count from the ideal case of a uniform grid consisting exclusively of equally-sized cubes without significantly compromising the accuracy in terms of wind flow and CHT. The main goal is to provide recommendations on how economical LES grids can be generated that still provide sufficient accuracy for engineering analysis. Without such recommendations, LES simulations of wind flow and CHT around buildings in an actual urban area will remain practically infeasible due to excessively large total numbers of cells and the associated excessive computational requirements. It should be stressed that coarser grids and the use of wall functions are generally not an option for accurate simulation of surface CHT in the complex flow field around bluff bodies such as buildings. Indeed, earlier research has shown that the use of wall functions can easily provide errors up to 60% in wall heat flux and that these errors can be avoided by proper high-resolution near-wall grids [7].

The structure of the present paper is as follows. In Section 2, the wind-tunnel experiments are briefly described. In Section 3, information on the computational models is presented. The CFD simulations are presented in Section 4. In Section 5, the limitations of the present study and prospects for future work are given. The main conclusions of this study and recommendations are presented in Section 6.

2. Description of wind-tunnel experiment

In this study, the experiments performed by Meinders [17] and Meinders et al. [18] are employed. In these experiments, the CHT at the surfaces of a wall-mounted cube placed in turbulent channel flow was evaluated. The channel in the experiments had a height of 0.05 m and a width of 0.6 m as shown in Fig. 1a. Measurements were performed for Reynolds numbers in the range of 2000 to 5000, based on the cube height ($H = 0.015$ m). Tripping strips were placed 0.75 m upstream of the cube to accelerate transition from a laminar to a turbulent boundary layer. The cube had a copper core with dimensions $12 \times 12 \times 12$ mm^3 around which an epoxy layer of thickness equal to 0.0015 m was applied on all surfaces as demonstrated in Fig. 1b. A dissipating source (resistance wire) placed inside the core was used to heat the copper core to a constant temperature of 75 °C. As a consequence of the high thermal conductivity of the copper, the interior of the epoxy layer was characterised by a uniform distribution of temperature. The thermal conductivity of the copper and epoxy were about 390 W/mK [17] and 0.24 W/mK [17,18], respectively. The temperature of the approach flow was maintained at a constant value of 21 °C for which the corresponding air thermal conductivity, density and dynamic viscosity were 0.026 W/mK, 1.225 kg/m^3 and 17.9×10^{-6} kg/ms, respectively. The external surface temperature distribution of the epoxy cube surface was measured with infrared thermography (IR). An IR camera was employed to detect the electromagnetic energy that was radiated in the IR spectral band from the object of interest. The electromagnetic energy was then converted into an electronic video signal [19]. In the experiments by Meinders [17] and Meinders et al. [18], the IR camera was mounted at 45-deg scan angle to enable capturing the lateral faces of the cube. The grid resolution of the infrared thermography measurements was 30×30 grid cells per cube surface [17]. In order to increase the accuracy of the IR measurements, the cube surface was coated with a thermal black paint of emissivity 0.95 to enhance thermal radiation. Afterwards, an in situ calibration was used to take into account the various environmental contributions (reflections and emissions [17]) and relate the local emitted intensity to the surface temperature distribution [17,18]. The heat balance between the heat conduction at the boundaries of the epoxy layer and the heat convection from the outer epoxy layer to the air yielded the local CHTC. As for the mean and instantaneous flow field characteristics around the wall-mounted cube, these were measured by a Laser Doppler Anemometry (LDA) system [17,18]. The measurement uncertainty of the surface temperature was

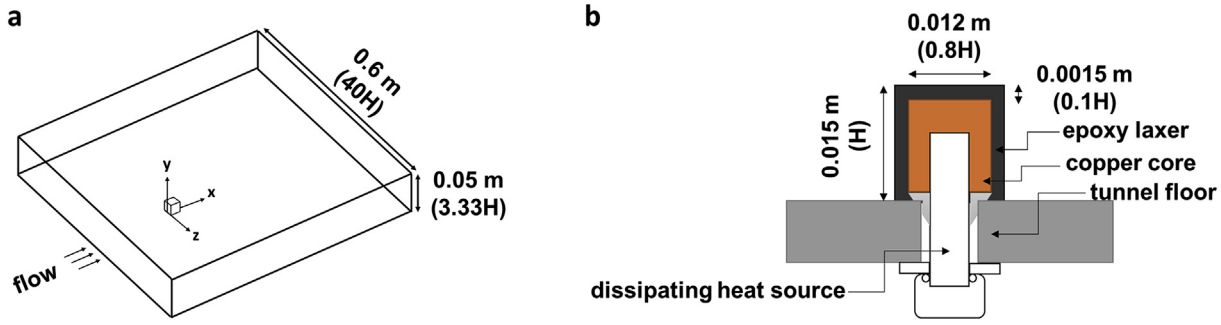

Fig. 1. Experimental setup (modified from Refs. [17,18]). (a) Perspective view of the wall-mounted cube in the channel and (b) vertical section through the heated cube.

estimated to be within ±0.4 °C, while the overall uncertainties for mean velocities and Reynolds stresses were approximately 5% and 10%, respectively [17,18].

Regarding the numerical analysis of this study, a Reynolds number of 4440 is considered since measured mean velocities and Reynolds stresses are available for the aforementioned Reynolds number. The corresponding averaged bulk velocity is 4.47 m/s (u_{ref}) and the average mass flow rate through the channel is 0.262 kg/s per unit area [17,18].

3. Computational set-up

3.1. Computational domain and grid

A computational domain of the cube (H = 0.015 m) including the epoxy layer is made with dimensions $L_D \times W_D \times H_D = 0.225 \times 0.315 \times 0.05\ m^3$ (Fig. 2). The cube is positioned at a distance of 4H (= 0.06 m) from the inlet plane. This value is smaller than the one recommended by Franke et al. [20] and Tominaga et al. [21], i.e. 5H, in order to limit the deterioration of the inlet profiles as mentioned by Blocken et al. [22,23]. The height of the domain is set equal to the height of the channel in the experiment (3.33H = 0.05 m). The width of the domain is set to 21H resulting in a blockage ratio of 1.4%, which is below the maximum value of 3.0% recommended by the aforementioned guidelines [20,21].

For the non-conformal grid, the domain is discretised in three subdomains $\Omega_{nc,1}$, $\Omega_{nc,2}$ and $\Omega_{nc,3}$ (Fig. 3). A 1:2 grid refinement ratio between the adjacent subdomains is used (Fig. 4a and b). For the subdomain $\Omega_{nc,1}$, the length of the cubic cells is H/40, resulting in a total number of 40 cubic cells to discretise the cube edges in all directions. In this case, 4 cells across the epoxy layer thickness are

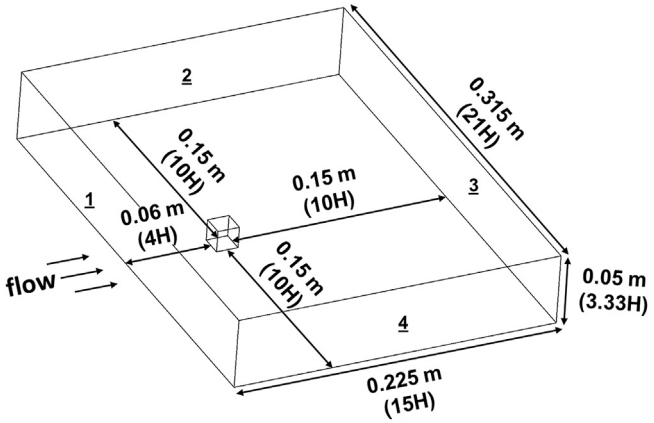

Fig. 2. Perspective view of the computational domain (H = 0.015 m).

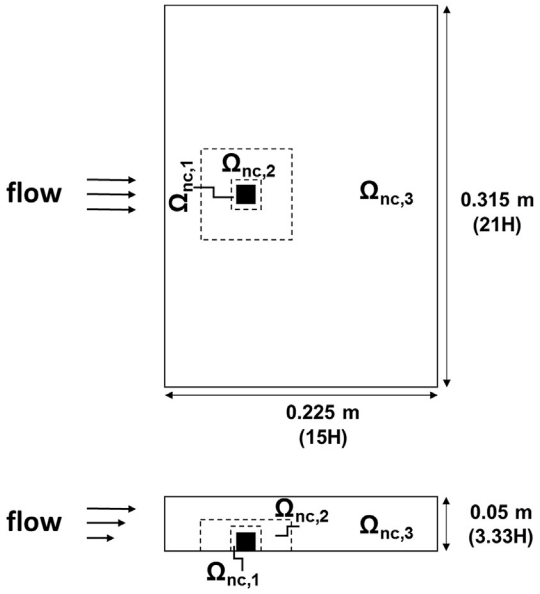

Fig. 3. Top and side view of the computational domain with indication of subdomains for non-conformal grid.

applied. This subdomain is extended up to a distance of approximately H/3 away from the cube surfaces. The subdomain $\Omega_{nc,2}$ consists of cubic cells with a length of H/20, extended up to a distance of approximately 1.8H away from the windward, leeward and side surfaces. Above the obstacle, the cubic cells of size H/20 are extended up to a height of 0.8H in order to limit the total number of cells. The rest of the domain ($\Omega_{nc,3}$) is discretised by cubic cells with a length of H/10. This results in a total cell count of 1,431,789 cubic cells.

For the conformal grid (Fig. 4c and d), a total number of 40 cubic cells is used for the cube surfaces in x-, y- and z-directions (with 4 cells across the epoxy layer thickness). The cubic cells are extended up to a distance of approximately 1.8H away from the windward, leeward and side surfaces. Similarly to the non-conformal grid, over the top surface of the cube the cells of size H/40 are extended up to a height of 0.8H. Beyond that region, a stretching ratio of 1.05 is applied to limit the total number of cells. In this case, the total number of cells is 9,710,472. Consequently, the conformal grid, as opposed to the non-conformal grid, does not consist entirely of cubic cells. In both cases, the distance from the centre point of the wall-adjacent cell to the wall for the cube surfaces is 1.88×10^{-4} m (y_p = H/80). In this case, the average value of the non-dimensional wall distance y^+ over all the cube surfaces is about 3.61 on both grids. Note that this is a rather large value that is

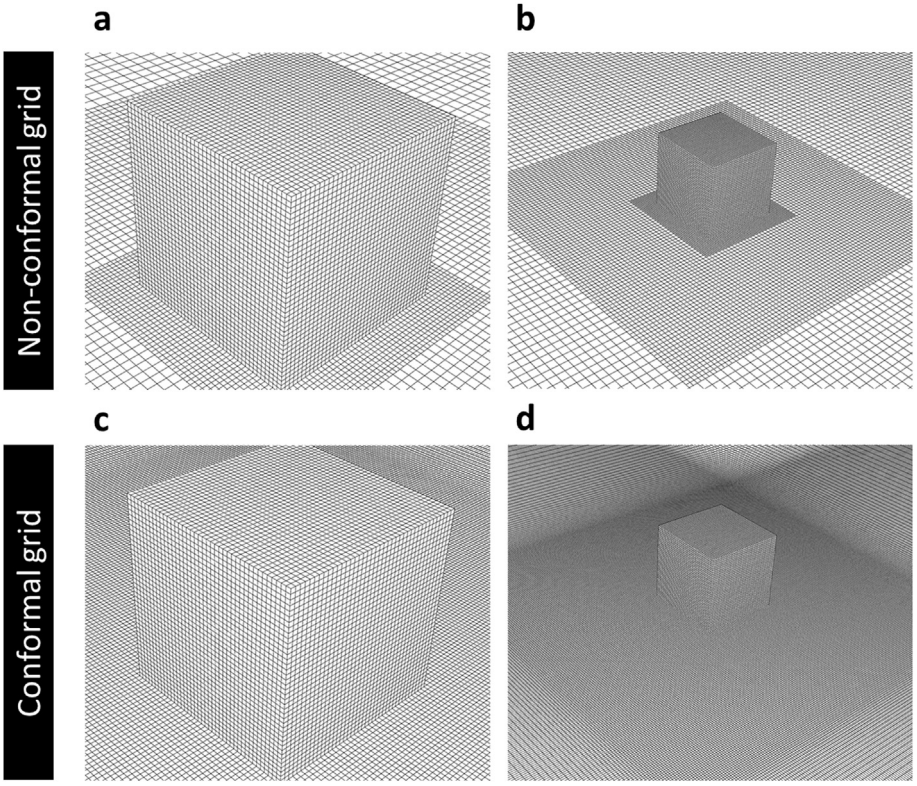

Fig. 4. (a,b) Perspective view of non-conformal grid at cube and part of the ground surface (total number of cells: 1,431,789). (c,d) Same for conformal grid (total number of cells: 9,710,472).

chosen in view of the intention of grid economy as explained at the end of Section 1.

3.2. Boundary conditions

In Fig. 2, planes 1 and 3 are the inlet and outlet planes, respectively, while planes 2 and 4 are the side planes. As the incident velocity profile is not given by Meinders [17] and Meinders et al. [18], this needs to be determined for the CFD simulations. In this study, the approach provided by Montazeri et al. [24] is used and a three-part profile is considered: a turbulent boundary layer near the bottom wall (part 1), a uniform core flow (part 2) and a laminar boundary layer (part 3) near the top wall of the domain. For the turbulent boundary layer, the air velocity changes from zero to 5.1 m/s (U_∞) at the height of 1.53H [17,18]. The velocity at the uniform core flow is equal to 5.1 m/s. At the laminar boundary layer, the velocity profile is defined as follows [25]:

$$\frac{u_3}{U_\infty} = \left[2\left(\frac{y}{H_3}\right) - \left(\frac{y}{H_3}\right)^2\right] \tag{1}$$

where H_3 is the laminar boundary layer thickness. In order to define the velocity profile, the heights of the second (H_2) and third (H_3) part of the profile need to be defined. These are determined based on the conservation of mass in the plane perpendicular to the flow: $\dot{m}_t = \dot{m}_1 + \dot{m}_2 + \dot{m}_3$, where $\dot{m}_t$ is the average mass flow rate in the channel (0.262 kg/s per unit area) and subscripts (1), (2) and (3) denote the mass flow rate of part 1, part 2 and part 3, respectively. As for the air mass flow rate of each part, this is determined based on the average velocity ($\rho\bar{u}_i H_i$). Note that for the laminar boundary layer, the average velocity is 2/3(U_∞). For turbulent kinetic energy k, a fitted profile based on the measurements is used. Further information on the implementation of the fitted profile for k can be found in Ref. [24]. The turbulence dissipation rate ε is given by Eq. (2):

$$\varepsilon(y) = \frac{u^{*3}}{\kappa(y + y_0)} \tag{2}$$

with the aerodynamic roughness length y_0 and friction velocity u^* being equal to 7.6×10^{-6} m and 0.25 m/s, respectively. The von Karman constant κ is considered to be 0.42.

Symmetry boundary conditions (zero normal velocity and zero normal gradients of all variables) are imposed at the sides of the domain. At the outlet, zero static gauge pressure is applied. The cube, ground surfaces and top of the domain are modelled as no-slip smooth walls. Note that no special treatment is applied to the ground surface to take into consideration the roughness. Nevertheless, as mentioned in Section 3.1, the inlet boundary is placed at a distance of 4H from the inlet plane in order to limit the appearance of longitudinal gradients in the boundary layer profiles [22,23]. In order to impose a time-dependent velocity profile at the inlet of the domain, the spectral synthesizer is adopted [26]. This inflow method provides a 3D transient velocity field based on the Fourier harmonics (number of harmonics: 100 [27]) with random coefficients following a normal distribution. The generated velocity fluctuation field is superimposed on the mean field.

The thermal boundary conditions are a fixed inlet air temperature (T_{in}) of 294 K (21 °C) and an adiabatic wall at the top and bottom of the computational domain. The surface temperature of the inner surface of the epoxy layer is fixed at 348 K (75 °C). Thermal conductivity of the epoxy and air is set as in the experiments [17,18], i.e. 0.24 W/mK and 0.026 W/mK respectively. At the bottom of the epoxy layer, a fixed value is used that is the average of

the surface temperature of the windward surface close to the ground plane and that of the copper core. Note that heat transfer across the cube surfaces is evaluated from the solution of temperature in the adjacent cells of the air and epoxy layer. For this study, the effect of buoyancy is neglected as the ratio of the Grashof number to Reynolds number squared (Gr/Re^2) is significantly smaller than one [17,18] and therefore only forced convection is considered. The Grashof number is defined as follows:

$$Gr = \frac{g\beta\Delta TH^3}{v^2} \quad (3)$$

where g (= 9.81 m/s^2) is the gravitational acceleration, β (= 0.003 K^{-1}) is the thermal expansion coefficient, ΔT (= 40 K) is the temperature difference between the surface and the ambient [17], H the height of the cube and v the kinematic viscosity.

3.3. Solver settings

For the simulations, the commercial CFD code ANSYS Fluent 15.0 is used [27]. All LES simulations are initialised with the solution of a preceding Reynolds-Averaged Navier-Stokes (RANS) simulation. For the 3D steady RANS simulations, the realizable k-ε turbulence model [28] is used together with the one-equation low-Re number Wolfshtein model [29]. For pressure-velocity coupling, the SIMPLE algorithm is used. Pressure interpolation is second order. Second-order discretisation schemes are used for both the convection and viscous terms of the governing equations.

For the LES, the standard Smagorinsky SGS model [30] with model constant C_s = 0.1 is employed. The bounded central-differencing scheme is used to discretise the convection term in the filtered momentum equation. Pressure-velocity coupling is performed using the fractional step method [31,32] in combination with the non-iterative time advancement (NITA) scheme, as outlined in Refs. [33–35]. For the NITA scheme, a single outer iteration for each time step is required while inner iterations are performed for each set of equations for momentum, pressure correction equation and energy equation until the convergence criterion is met. In this case each set of equations is segregated from each other and solved independently one by one. As opposed to the iterative time advancement (ITA), which requires a considerable number of outer iterations, the use of the NITA scheme significantly reduces the computational time [27,36]. Time discretisation is second-order implicit. Two time steps are used: $\Delta t_1 = 8 \times 10^{-4}$ s and $\Delta t_2 = 4 \times 10^{-5}$ s. The reason for selecting a higher time step (Δt_1) is to speed up the development of the net heat flux in the epoxy layer. The LES are performed with Δt_1 until the net heat flux into the epoxy layer reaches approximately 0.02 W, indicating that the energy conservation between the boundaries of the epoxy layer is sufficiently met. The aforementioned condition is achieved after approximately 530 flow-through-times ($t_{ft} = L_D/u_{ref}$). Then, the simulations are continued with Δt_2 maintaining the Courant number (CFL) below one. The LES initialisation period with Δt_2 lasts approximately T_{init} = 0.72 s corresponding to 14.3 flow-through times. After the initialisation period, the statistics are sampled for T_{avg} = 2.8 s, corresponding to 55.6 flow-through times.

All simulations are performed on the HPC cluster at the Department of the Built Environment of the Eindhoven University of Technology, the Netherlands. A 12-core node is used (Intel(R) Xeon(R) CPU - X5650 @ 2.67 GHz) with 96 GB of system memory and x86_64 architecture.

4. Computational simulation results

4.1. Monitoring of statistical convergence

In Fig. 5a, the evolution of the non-dimensional moving-average of the mean streamwise velocity is shown as a function of the number of flow-through times in the sampling/averaging period (70,000 time steps) in three monitoring points in the fluid zone for the LES computation on the non-conformal grid. The same evaluation is performed for the moving-average of the temperature in one monitoring point (Fig. 5b) in the fluid zone and three monitoring points in the solid zone of the epoxy layer (Fig. 5c). For this part of the analysis, the 70,000 time steps of the averaging period

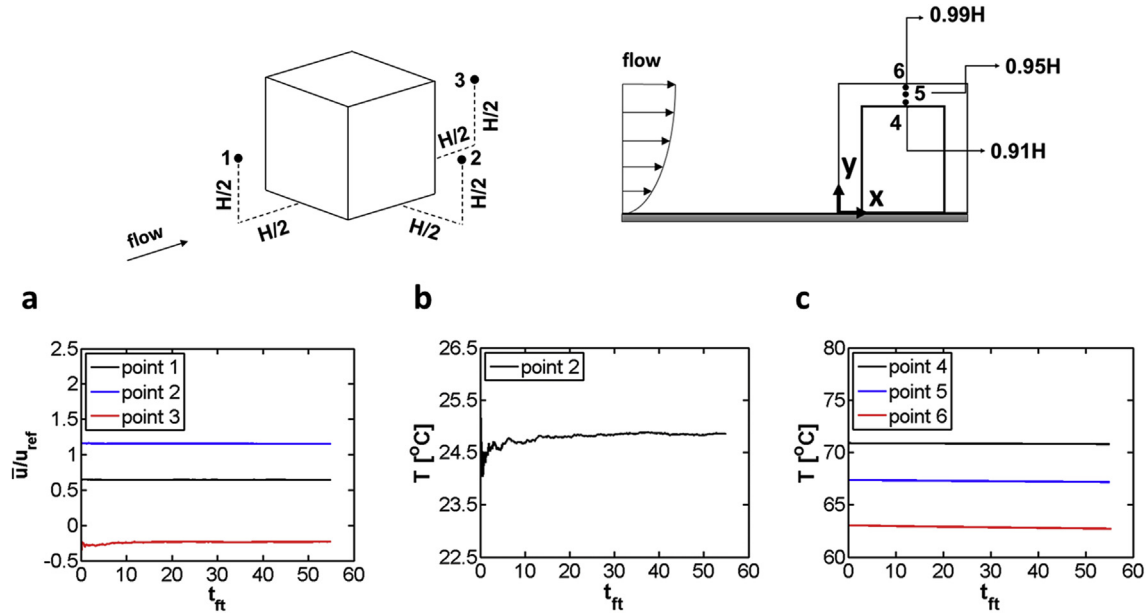

Fig. 5. Convergence monitoring: moving-average (over 70,000 time steps) as a function of number of flow-through times in the averaging period: (a) non-dimensional mean streamwise velocity in three points; (b) temperature in one point in the fluid zone; (c) temperature in three points in the solid zone.

Table 1
Convergence monitoring: e_{conv} (%) at point 1, point 2 and point 3 in the fluid zone and point 4, point 5 and point 6 in the solid zone for seven successive equal ranges of time step in the averaging period.

Range of time step	$\overline{u}/u_{ref}$			T			
	point 1	point 2	point 3	point 2	point 4	point 5	point 6
1–10,000	2.31	2.49	65.59	15.03	0.03	0.04	0.10
10,001–20,000	0.32	0.13	7.12	0.66	0.02	0.04	0.09
20,001–30,000	0.26	0.09	2.54	0.29	0.02	0.04	0.06
30,001–40,000	0.11	0.09	2.97	0.23	0.02	0.04	0.07
40,001–50,000	0.09	0.09	2.53	0.15	0.02	0.04	0.07
50,001–60,000	0.05	0.04	1.74	0.20	0.02	0.04	0.07
60,001–70,000	0.07	0.04	1.62	0.16	0.02	0.04	0.07

are divided into seven equal intervals. For each value, the convergence is quantified by e_{conv} (%) for a given range of time steps I as follows:

$$e_{conv}(I) = \frac{|Q_{max} - Q_{min}|}{|Q_{avg}|} \times 100 \quad (4)$$

where Q_{max} and Q_{min} are the maximum and minimum values of a flow variable within an interval I of time steps in the averaging period. Q_{avg} is the final average value. The values of e_{conv} are reported in Table 1 for the monitoring points in the fluid and solid zone. The influence of the instantaneous flow patterns can be observed at the beginning of the averaging period, especially in point 3 which is located in the wake of the cube. In this case e_{conv} presents a high value of 65.59%. However, at the end of the averaging period (I = 7), e_{conv} has decreased and reaches relatively low values (≤1.62%) indicating sufficient statistical convergence of the simulation. In Section 4.2 and Section 4.3, the LES results on the non-conformal grid represent the averaged values of the quantities over I = 7.

The LES computation on the conformal grid is terminated when the moving average of the mean streamwise velocity (points 1, 2 and 3) and temperature (points 2, 4, 5 and 6) remains within 1.35%.

4.2. Comparison between results on non-conformal and conformal grid

In this section, the LES results obtained on the non-conformal and conformal grid are presented and compared. Fig. 6 shows the profiles of normalised mean streamwise velocity $\overline{u}/u_{ref}$ along nine lines at the top, in the wake and at the side of the cube. The difference between the results of both cases is relatively small. The average absolute deviation along all lines is about 0.033. The highest discrepancies are found in the recirculation area, at the side of the cube, where the absolute deviation on the non-conformal grid goes up to 0.35 compared to the conformal grid. This discrepancy is attributed to the coarser resolution that is used at the upstream fetch of the cube on the non-conformal grid compared to the conformal grid. Fig. 7 presents profiles of normalised mean streamwise velocity at a distance of 2H (subdomain $\Omega_{nc,3}$) and 1.5H (subdomain $\Omega_{nc,2}$) upstream of the windward surface of the cube for both LES computations. In this case, acceleration of the flow close to the ground surface is observed for the LES computation on the non-conformal grid, in subdomain $\Omega_{nc,3}$. However, the acceleration on the non-conformal grid becomes less pronounced compared to the conformal grid after the transition to subdomain $\Omega_{nc,2}$.

Fig. 8 provides the profiles of normalised Reynolds stresses $\overline{u'^2}/u^2_{ref}$ along nine lines at the top, in the wake and at the side of the cube. At the top and side of the cube, the LES on the non-conformal grid presents an average absolute deviation of 0.0016 compared to the conformal grid. In the wake of the cube, the absolute deviation increases to about 0.0021. In contrast to the mean streamwise velocity, discontinuities in the profiles of $\overline{u'^2}/u^2_{ref}$ on the non-conformal grid are observed at approximately x/H = 2.8 along the three lines in the wake. This is the position where the intersection between $\Omega_{nc,2}$ and $\Omega_{nc,3}$ is positioned. At the top and side of the cube no discontinuities are present. This observation is in line with the findings of Piomelli et al. [15], who reported significant decrease in resolved stresses only in cases where the non-conformal interfaces are normal to the direction of the mean flow. A possible explanation for this behaviour is insufficient resolution of the resolved eddies on the coarse grid, but also aliasing and numerical errors due to interpolation and flux reconstruction [15]. In addition, the observed overshoots of the resolved normalised Reynolds stresses immediately before the non-conformal interface of the subdomains $\Omega_{nc,2}$ and $\Omega_{nc,3}$ correspond to the accumulation of energy at the small scales as observed by Vanella et al. [16]. Finally, despite the energy pile-up before the $\Omega_{nc,2}$ - $\Omega_{nc,3}$ interface, the flow adjusts quickly to the grid coarsening [16].

The profiles of surface temperature along lines at the intersection of the cube and planes z/H = 0 and y/H = 0.5 are presented in Fig. 9a and Fig. 9b, respectively. An average absolute difference of surface temperature on all surfaces of the cube of about 0.9% (0.5 °C) is observed, between the two LES simulations. The most pronounced discrepancy of 4.4% (2.1 °C) is found at the leeward surface.

Fig. 10 provides a comparison of the main flow features between the experimental results and the LES results on the non-conformal and the conformal grid. Upstream of the windward surface, a difference of 0.09H is observed for the position of the separation saddle point S_b (L_{F1}), which is attributed to the difference in the approach-flow profile shown in Fig. 7. The stagnation point on the windward surface is found at a height of 0.70H (L_{F2}) for both simulations, which is also in good agreement with the measurements. The flow reattaches downstream of the leeward surface (marked C) at a length, L_{R1}, of 1.53H for the simulation on the non-conformal grid. On the conformal grid, this value is 1.54H. No qualitative discontinuities are observed on the non-conformal interfaces (Fig. 10).

Table 2 presents the computational expense in terms of Central Processing Unit (CPU) hours required by the LES on the non-conformal and conformal grid. It can be seen that the LES on the non-conformal grid required approximately 8.5 times less CPU hours than the LES on the conformal grid. Note that the difference in total cell count is of 6.8 (Table 2).

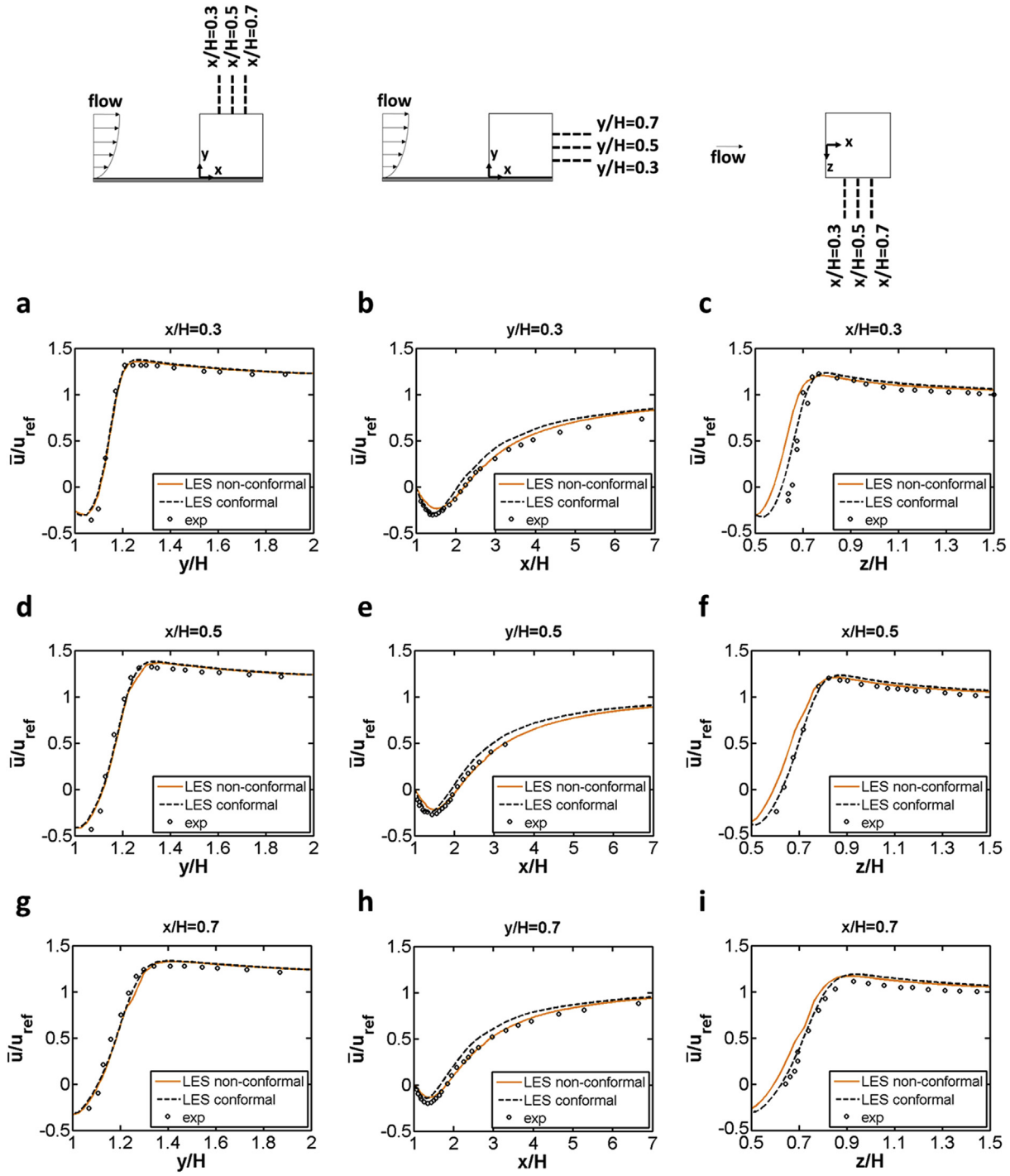

Fig. 6. Comparison of numerical and experimental results of normalised mean streamwise velocity distribution along lines (a,d,g) at the top (plane z/H = 0), (b,e,h) in the wake (plane z/H = 0) and (c,f,i) at the side (plane y/H = 0.5) of the cube.

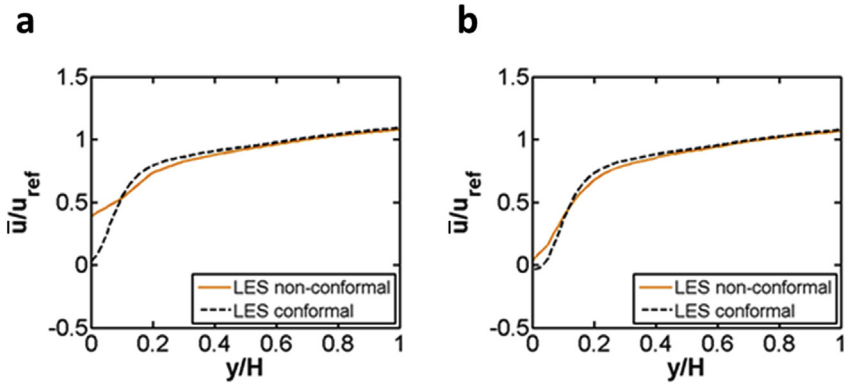

Fig. 7. Normalised mean streamwise velocity distribution along lines at the plane z/H = 0 and at a distance of (a) x/H = 2H and (b) x/H = 1.5H upstream of the windward surface of the cube. Comparison between LES on non-conformal and conformal grid.

4.3. Comparison with wind-tunnel experiments

The LES results on the non-conformal grid are compared with the experimental data by Meinders [17] and Meinders et al. [18]. In order to quantify the agreement between the numerical and experimental results, the validation metrics fraction of prediction within a factor of 1.05 and 1.3 (FAC1.05 and FAC1.3), normalised mean square error (NMSE) and hit rate (q) are used.

Fraction of prediction within a factor 1.05 (FAC1.05) and 1.3 (FAC1.3) count the fraction of data points of which the predictions are respectively within a factor of 1.05 and 1.3 of the observations, based on the ratio of the predicted and observed values [37]:

$$\mathrm{FAC1.05} = \frac{1}{N}\sum_{i=1}^{N} n_i \quad \text{with} \quad n_i = \begin{cases} 1 & \text{for } 0.95 \le \dfrac{P_i}{O_i} \le 1.05 \\ 0 & \text{else} \end{cases} \tag{5}$$

$$\mathrm{FAC1.3} = \frac{1}{N}\sum_{i=1}^{N} n_i \quad \text{with} \quad n_i = \begin{cases} 1 & \text{for } 0.77 \le \dfrac{P_i}{O_i} \le 1.30 \\ 0 & \text{else} \end{cases} \tag{6}$$

The normalised mean square error (NMSE) is a measure of the scatter of the data. The square brackets indicate averaging over all the measurement points [37]:

$$\mathrm{NMSE} = \frac{[(O-P)^2]}{[O][P]} \tag{7}$$

where P and O are the predicted values and the observed/experimental value, respectively.

The hit rate (q) specifies the fraction of predicted results that are different, within an allowed range D_q or W_q, from the experimental data [37]:

$$q = \frac{1}{N}\sum_{i=1}^{N} n_i \quad \text{with} \quad n_i = \begin{cases} 1 & \text{for } \left|\dfrac{P_i - O_i}{O_i}\right| \le D_q \text{ or } |P_i - O_i| \le W_q \\ 0 & \text{else} \end{cases} \tag{8}$$

where P_i and O_i are the predicted values and the experimental values of a given variable for the data point i, respectively; N is the number of data points; D_q and W_q are the allowed relative and absolute deviations, respectively. The ideal values of the metrics that correspond to perfect agreement are 1 for FAC1.05, FAC1.3 and q, and 0 for NMSE. Note that NMSE cannot be used for variables that can receive both negative and positive values and therefore is not used for the analysis of normalised mean streamwise velocity. The values of the relative and absolute error thresholds for q are taken equal to $D_q = 0.25$ and $W_q = 0.04$ for normalised mean streamwise velocity and $D_q = 0.25$ and $W_q = 0.004$ for normalised Reynolds stresses, respectively. The threshold for absolute and relative error is based on the uncertainty of the experiment [17,18] and Ref. [38], respectively.

4.3.1. Flow field

Fig. 6 compares the CFD results and the experimental results of normalised mean streamwise velocity along the nine lines at the top, in the wake and at the side of the cube. The simulations are capable of accurately reproducing the reverse flow at the top (FAC1.3 = 0.80 and q = 0.78) and side (FAC1.3 = 0.72 and q = 0.75) of the cube. In the wake (Fig. 6b, e and h), LES slightly over-predicts the experimental results close to the surface but in general it retains its good performance (FAC1.3 = 0.75 and q = 0.76).

At the top (Fig. 8a, d and g) and side (Fig. 8c, f and i) of the cube, the profiles of normalised Reynolds stresses present certain discrepancies. In this case, the local maxima of the measurements are under-predicted by the LES. However, the agreement remains fairly good with FAC1.3 = 0.23, NMSE = 0.40 and q = 0.50 at the top and FAC1.3 = 0.28, NMSE = 0.27 and q = 0.53 at the side of the cube. A general good agreement is observed in the wake zone (FAC1.3 = 0.87, NMSE = 0.03 and q = 0.93).

The validation metrics over all the measurement points are reported in Table 3 for the LES on the non-conformal and conformal grid. The validation metrics on the non-conformal and conformal grid are very similar.

4.3.2. Surface temperature

In Fig. 9, the distribution of surface temperature shows lower values near the top edge of the windward surface. At the lower part of the surface, the region where the centre of the horseshoe vortex is found, the surface temperature is overestimated reaching 59.5 °C compared to 56.8 °C in the measurements [17,18]. Possible explanations for this observation are the additional heat loss of the epoxy layer through the tunnel floor (Fig. 1b) in the experiments, which is not considered in the simulations [17,18], and the different position of the horseshoe vortex in LES simulation versus experiments (Fig. 10). The average absolute deviation for the windward surface is 1.83%. For the top and side of the cube, where flow separation and reattachment are very complex and intermittent, a large streamwise gradient is observed. In the regions of reversed flow, the

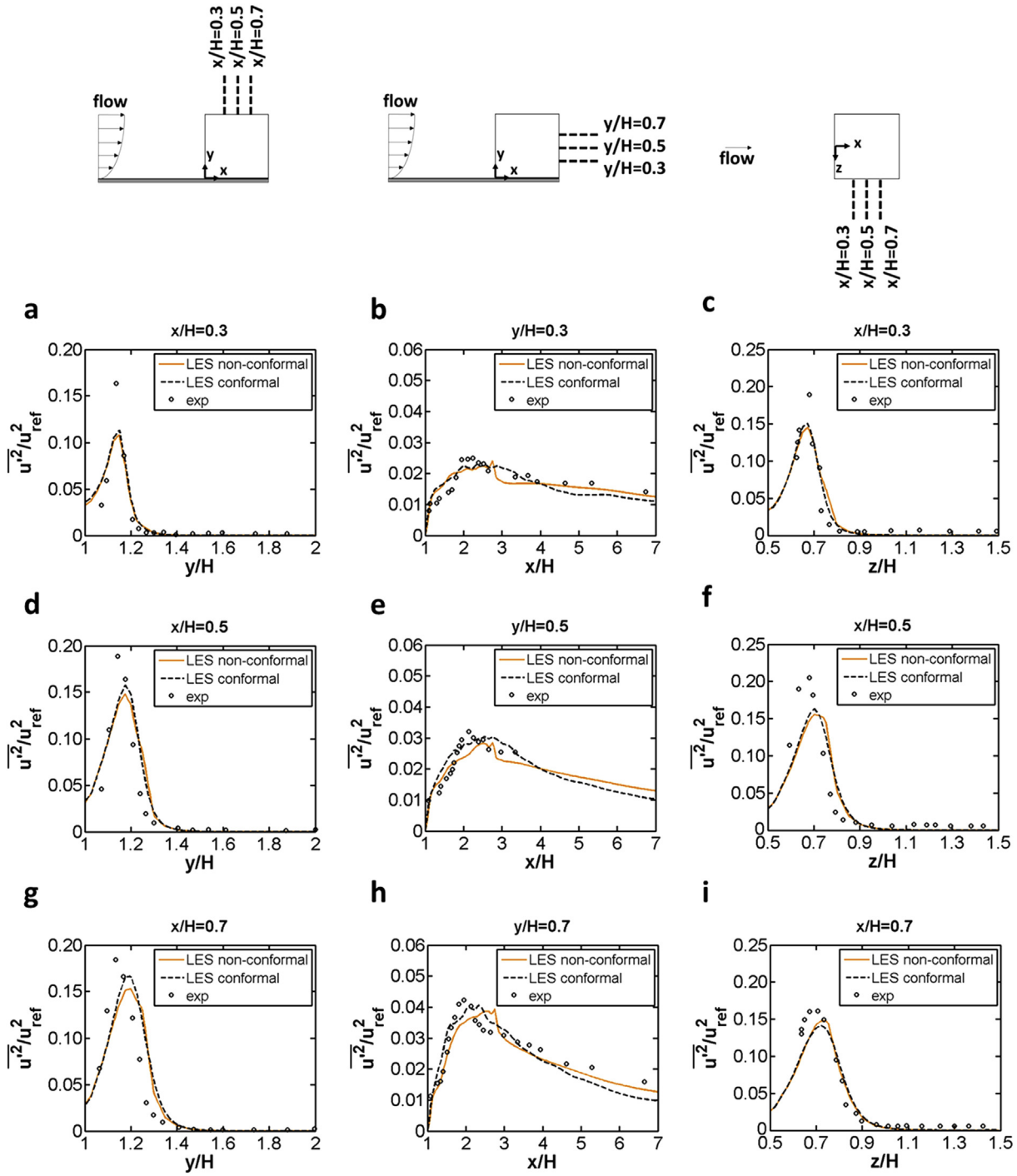

Fig. 8. Comparison of numerical and experimental results of normalised Reynolds stresses distribution along lines (a,d,g) at the top (plane z/H = 0), (b,e,h) in the wake (plane z/H = 0) and (c,f,i) at the side (plane y/H = 0.5) of the cube.

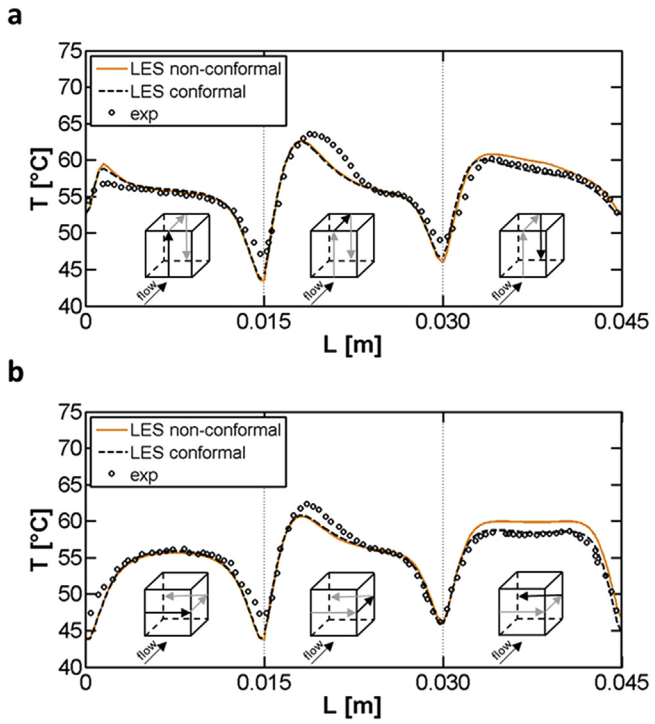

Fig. 9. (a,b) Comparison of numerical and experimental results of surface temperature along lines on cube surfaces.

simulated surface temperature drops to lower values compared to the experimented ones. This behaviour can be associated with the different values of the Reynolds stresses obtained by LES, close to the cube surfaces, on top and at the side of the cube. The resulting average absolute deviation of surface temperature on top and side surface is 2.06% and 1.63%, respectively. For the leeward surface of the cube, an almost uniform distribution of the surface temperature is observed due to the efficient mixing caused by the recirculation of the flow in the wake of the cube [17,18]. Although the simulated surface temperatures are slightly higher compared to the measurements, the average absolute deviation for the leeward surface is 2.17%.

The average and maximum absolute deviation in surface temperature along all lines are 2.0% (1.1 °C) and 7.6% (3.6 °C), respectively. For the validation metrics, FAC1.05 = 0.92 and NMSE reaches a small value of 0.0013 as shown in Table 3.

Table 2
Comparison of grid size and CPU hours required by LES on the non-conformal and conformal grid.

Grid	Grid size (cells)	CPU hours
Non-conformal	1,431,789	2188
Conformal	9,710,472	18,539

4.4. Sensitivity analysis

A systematic sensitivity analysis is conducted on the non-conformal grid by varying a single grid characteristic compared to

Table 3
Validation metrics for the LES on the non-conformal and conformal grid for $\overline{u}/u_{ref}$, $\overline{u'^2}/u_{ref}^2$ and T.

	$\overline{u}/u_{ref}$		$\overline{u'^2}/u_{ref}^2$			T	
	FAC1.3	q	FAC1.3	NMSE	q	FAC1.05	NMSE
Ideal value	1	1	1	0	1	1	0
LES non-conformal	0.76	0.76	0.46	0.23	0.65	0.92	0.0013
LES conformal	0.79	0.77	0.48	0.24	0.66	0.93	0.0010

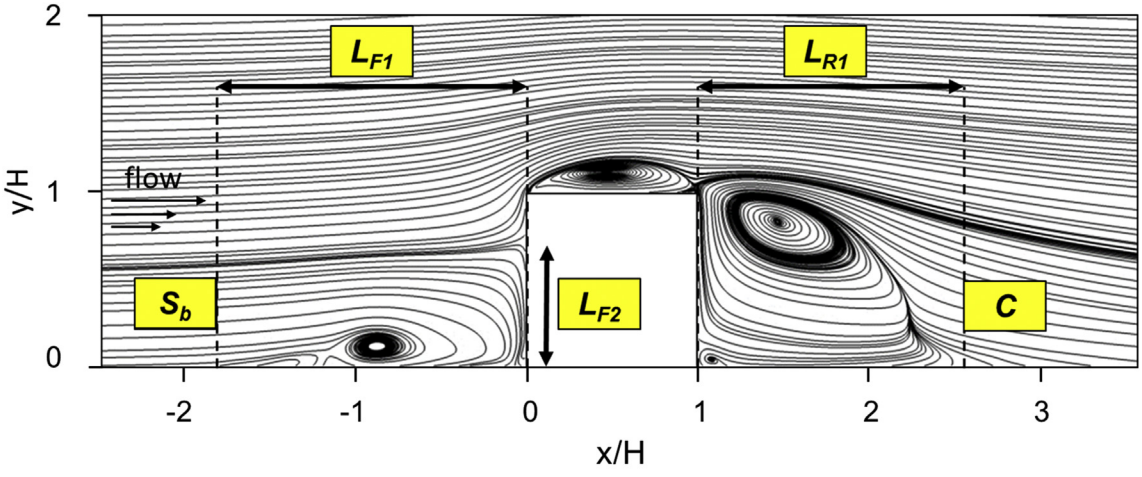

Case	L_{F1}	L_{F2}	L_{R1}
LES non-conformal	1.76H	0.70H	1.53H
LES conformal	1.67H	0.70H	1.54H
Exp.	1.40H	0.67H	1.50H

Fig. 10. Comparison of the main flow features around the cube obtained by the LES on the non-conformal and conformal grid and by experiments [17,18]. Streamlines obtained by LES on the non-conformal grid.

Table 4
Average absolute deviations (−) between LES of Section 4.4 and reference case for normalised mean streamwise velocity, normalised turbulent kinetic energy and normalised local air temperature. The subscript (rc) denotes the quantity obtained by the reference case.

Grid characteristic	Case	Grid size (cells)	$\frac{\lvert\overline{u}-\overline{u}_{rc}\rvert}{u_{ref}}$	$\frac{\lvert k-k_{rc}\rvert}{u_{ref}^2}$	$\frac{\lvert T_{fluid}-T_{fluid,rc}\rvert}{T_{wall}-T_{in}}$
Grid resolution (Section 4.4.1)	LES non-conf. 30	622,370	0.080	0.0040	0.0059
	LES non-conf. 50	2,888,800	0.090	0.0050	0.0054
Subdomain ($\Omega_{nc,2}$) size (Section 4.4.2)	LES non-conf. H	1,259,000	0.069	0.0019	0.0016
	LES non-conf. 3H	1,819,000	0.066	0.0018	0.0005
Grid refinement ratio (Section 4.4.3)	LES non-conf. 1:3	320,526	0.070	0.0050	0.0073
	LES non-conf. 1:4	206,416	0.030	0.0060	0.0032

Table 5
Average absolute deviations (%) between LES of Section 4.4 and reference case for CHTC along the cube surfaces. The subscript (rc) denotes the quantity obtained by the reference case.

Grid characteristic	Case	Grid size (cells)	$\frac{\lvert CHTC-CHTC_{rc}\rvert}{CHTC_{rc}}$ x 100						
			Windward		Top	Side	Leeward		Overall
			Intersection of the cube and z/H = 0	Intersection of the cube and y/H = 0.5			Intersection of the cube and z/H = 0	Intersection of the cube and y/H = 0.5	
Grid resolution (Section 4.4.1)	LES non-conf. 30	622,370	8.3	13.9	13.0	11.8	4.7	7.1	9.8
	LES non-conf. 50	2,888,800	5.8	8.9	12.1	6.5	4.6	3.2	6.9
Subdomain ($\Omega_{nc,2}$) size (Section 4.4.2)	LES non-conf. H	1,259,000	1.7	1.1	2.2	0.6	4.3	3.0	2.2
	LES non-conf. 3H	1,819,000	0.7	1.5	1.1	0.8	1.2	1.4	1.1
Grid refinement ratio (Section 4.4.3)	LES non-conf. 1:3	320,526	3.8	4.4	12.5	9.0	3.7	4.8	6.4
	LES non-conf. 1:4	206,416	6.1	9.8	2.5	8.0	1.9	6.7	5.8

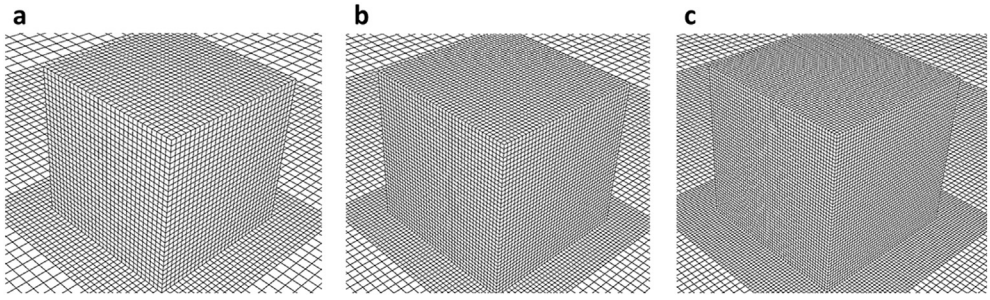

Fig. 11. Computational grids for grid resolution analysis. (a) Coarse grid (total number of cells: 622,370); (b) basic grid (total number of cells: 1,404,653); (c) fine grid (total number of cells: 2,888,800).

the reference case. The reference case is the one used in the foregoing sections, with 40 cells per cube edge, 1.8H of subdomain size and 1:2 grid refinement ratio. The impact of the overall resolution of the grid, the size of the middle subdomain ($\Omega_{nc,2}$), and the refinement ratio between adjacent subdomains on the CFD results is investigated. The same computational parameters as reported in Section 3 are used. To accelerate the simulations, the epoxy layer is not considered in these simulations and a constant temperature boundary condition (T_{wall} = 75 °C) is imposed at the exterior surface of the cube. In this case, LES for the reference case is performed on a grid with 1,404,653 cubic cells. For each of the following sections, a comparison between the results of the LES on the additional non-conformal grids and that of the reference case is carried out. For each comparison, the average absolute deviation of normalised mean streamwise velocity $\overline{u}$, normalised turbulent kinetic energy k and normalised local air temperature T_{fluid} along nine lines, as demonstrated in Figs. 6 and 8, is calculated and presented in Table 4. In addition, average absolute deviations of CHTC across all the surfaces of the cube are reported in Table 5.

4.4.1. Impact of grid resolution

Two additional grids are constructed, a coarser and a finer one, in order to evaluate the impact of grid resolution. For the coarse and fine grid, a total number of 30 and 50 cubic cells are used to discretise the cube edges in all directions, respectively. This results in grids with 622,370 and 2,888,800 cubic cells, respectively. The

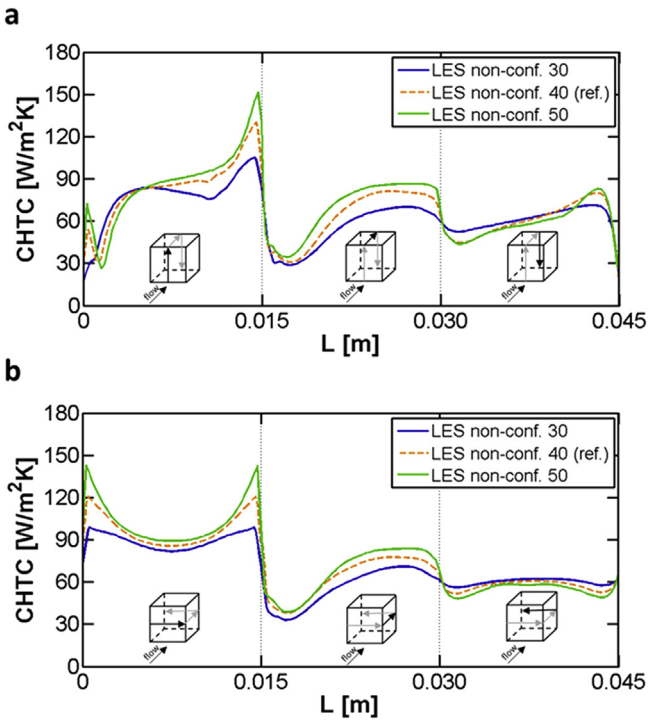

Fig. 12. The impact of grid resolution: (a,b) CFD results of CHTC along lines on the cube surfaces.

three grids are shown in Fig. 11.

The results for CHTC, on the three grids, along lines at the intersection of the cube and planes z/H = 0 and y/H = 0.5 are compared in Fig. 12. The comparison of the results of the reference case (basic grid) with the coarse and fine grid shows an average absolute deviation of 9.8% and 6.9%, respectively. At the windward surface, the use of a finer grid yields local overestimations of CHTC up to 40.3% compared to the reference case while the coarser grid shows, as a result of the larger y^+, underestimation up to 70.3%. For the top and side surface of the cube, the LES on the coarse and fine grid present lower and higher values of normalised turbulent kinetic energy (Fig. 13), respectively, compared to the reference case. Consequently, the CHTC receives higher values on the fine grid and lower on the coarse grid in those regions. On average, the absolute deviation for CHTC at the top surface is 13.0% and 12.1% on the coarse and fine grid respectively, while at the side surface this is 11.8% and 6.5%. At the leeward surface a reverse behaviour for the turbulent kinetic energy (Fig. 13b, e and h) is observed. In this case, the results show that the LES on the coarse grid presents higher values of turbulent kinetic energy. As a result, higher values of CHTC are observed compared to the ones obtained on the reference case and fine grid. This behaviour is reported in an earlier study [39] and is attributed to the low values of the resolved strain rate tensor S_{ij}, due to the coarse resolution, which results in higher resolved turbulent kinetic energy in the wake of the cube. In this case, the average absolute deviation of CHTC compared to the reference case is 5.9% and 3.9% on the coarse and fine grid respectively.

The analysis above shows that grid resolution has a significant impact on the results for the flow field and CHTC, while the increase of the grid resolution presents a decrease of the discontinuities in the profiles of normalised turbulent kinetic energy. Although the use of 50 cells per cube edge results in large local overestimations in CHTC, compared to the reference case, the average deviation is of 6.9%. It is therefore concluded that the use of 40 cells per cube edge (reference case) provides sufficient resolution for the analysis of the flow field and CHTC.

4.4.2. Impact of subdomain size

In this section, the impact of the size of the middle subdomain, $\Omega_{nc,2}$ (Fig. 3), on the CFD results is evaluated. Two additional grids are constructed in which the middle subdomain $\Omega_{nc,2}$ is extended up to a distance of H and 3H (Fig. 14) away from the windward, leeward and side surfaces, resulting in a total number of 1,259,000 and 1,819,000 cells, respectively. Note that for both cases, the size of the subdomain $\Omega_{nc,2}$ over the cube is kept the same as the reference case, i.e. 0.8H. The average absolute deviations presented in Table 4 show that the simulations on the two additional grids only present small deviations with the reference case for normalised mean streamwise velocity $\overline{u}$, normalised turbulent kinetic energy k and normalised local air temperature T_{fluid}.

Fig. 15 shows the CHTC distribution along lines at the intersection of the cube and planes z/H = 0 and y/H = 0.5. The results of CHTC between the three LES are very similar indicating negligible sensitivity to the size of the middle subdomain within the range investigated. The average absolute deviation between the reference case and the LES where $\Omega_{nc,2}$ is extended up to H is 2.2%. It is 1.1% when $\Omega_{nc,2}$ is extended up to 3H. This similarity is also confirmed by the coinciding profiles of normalised turbulent kinetic energy close to the cube (Fig. 16). Noteworthy is that the transition to the coarsest resolution at different locations between the three cases i.e. H, 1.8H and 3H downstream of the trailing surface, has a direct effect on the turbulent kinetic energy, indicating thus dependence on the position of the $\Omega_{nc,2}$ - $\Omega_{nc,3}$ interface. This can be seen in Fig. 16b, e and h where close to the non-conformal interfaces, the results show a sudden decrease. In this case, the sudden decrease is dependent on the difference between the resolved turbulence obtained on the fine (subdomain $\Omega_{nc,2}$) and coarse resolution (subdomain $\Omega_{nc,3}$) of the fine-coarse interface. Further downstream of the trailing surface, however, at a distance of approximately x/H = 4.2, the three profiles present similar values of normalised turbulent kinetic energy.

It is clear that, within the range investigated, the impact of subdomain size is negligible with respect to the results for CHTC. As for turbulent kinetic energy, significant deviations are observed only after the $\Omega_{nc,2}$ - $\Omega_{nc,3}$ interface, whilst close to the cube surfaces deviations are small. Therefore, it is concluded that a subdomain size equal to H can be used and a reduction of the total cell count by a factor of 7.7 (compared to a conformal grid) is achieved.

4.4.3. Impact of grid refinement ratio between adjacent subdomains

In this section, the impact of the grid refinement ratio between adjacent subdomains is evaluated. Two supplementary grids are constructed with a grid refinement ratio 1:3 (Fig. 17b) and 1:4 (Fig. 17c) between adjacent subdomains. The resulting total number of cells is 320,526 and 206,416 cells, respectively.

The results of the CHTC distribution are shown in Fig. 18. The average absolute deviation between the results on the grid with refinement ratio 1:4 and the reference case (i.e. 40 cells per cube edge, 1.8H of subdomain size, 1:2 grid refinement ratio) is about 5.8%. This is about 6.4% for refinement ratio 1:3. The CHTC profiles at the windward surface show that the use of grid refinement ratio 1:3 can yield a local maximum absolute deviation of 18.0%, compared to the reference case, while for 1:4 this is 58.4%. Fig. 19 shows the profiles of normalised turbulent kinetic energy. At the top and side surface of the cube the LES with grid refinement ratio 1:4 presents similar values as the reference case while underestimations are observed for 1:3. Average absolute deviations in CHTC of 12.5% and 2.5% are observed at the top for LES with refinement ratio 1:3 and 1:4, respectively. At the side, the absolute deviations are 9.0% and 8.0%, respectively. For the leeward surface,

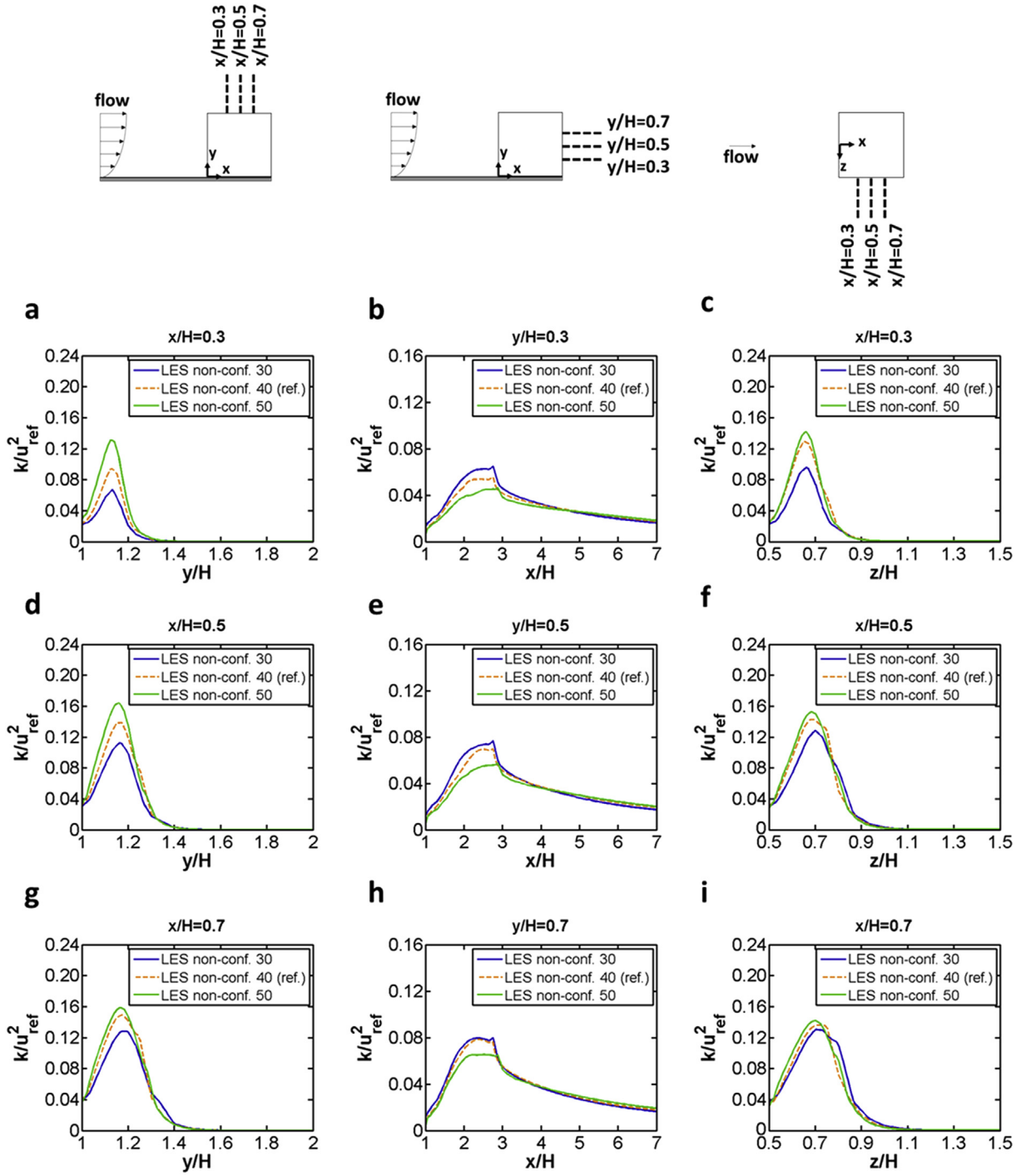

Fig. 13. The impact of grid resolution: CFD results of normalised turbulent kinetic energy along lines (a,d,g) at the top (plane z/H = 0), (b,e,h) in the wake (plane z/H = 0) and (c,f,i) at the side (plane y/H = 0.5) of the cube.

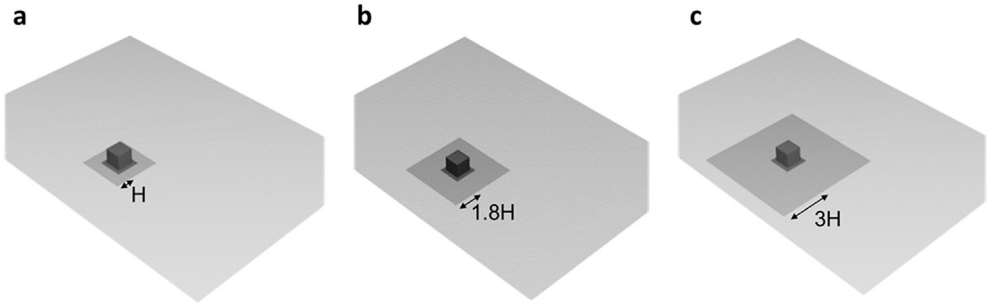

Fig. 14. Computational grids for subdomain size analysis. Subdomain size: (a) H (total number of cells: 1,259,000); (b) 1.8H (total number of cells: 1,404,653); (c) 3H (total number of cells: 1,819,000).

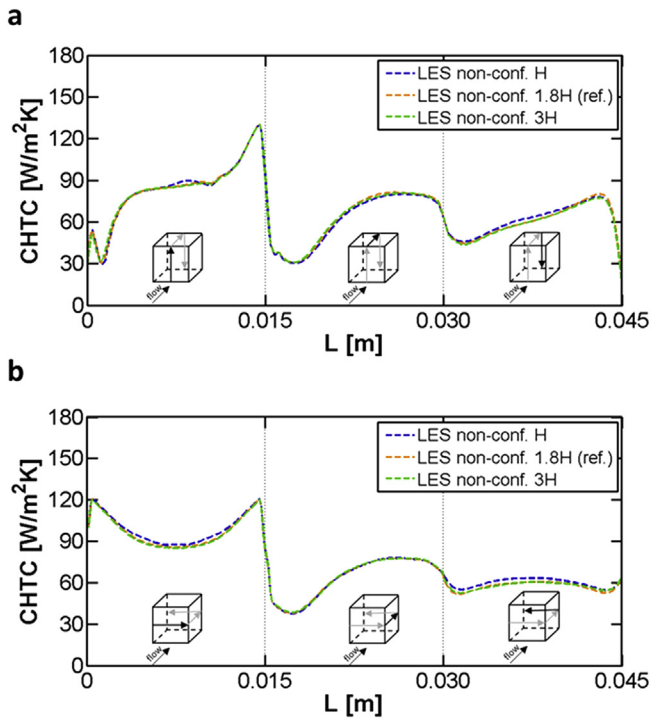

Fig. 15. The impact of subdomain size: (a,b) CFD results of CHTC along lines on the cube surfaces.

both simulations present an average absolute deviation of 4.3% with the reference case. It should be noted that, downstream of the cube, at the position where the transition to the coarsest grid is found, the results of normalised turbulent kinetic energy (Fig. 19b, e and h) indicate sensitivity to the grid refinement ratio. In this case, as the refinement ratio increases, larger overshoots immediately before the interface $\Omega_{nc,2}$ and $\Omega_{nc,3}$ and larger drops (immediately after interface $\Omega_{nc,2}$ and $\Omega_{nc,3}$) in the profiles of normalised turbulent kinetic energy are observed.

The analysis of the impact of grid refinement ratios 1:3 and 1:4 between adjacent subdomains shows similar average absolute deviations of CHTC when compared to the reference case. Despite this observed similarity, the use of grid refinement ratio 1:4 can, however, lead to significantly larger deviations for CHTC on the windward surface compared to 1:3. In addition, the increase of grid refinement ratio to higher than 1:3 is accompanied with augmented discontinuities of turbulent kinetic energy profiles and energy pile-up downstream of the cube. Consequently, the use of a ratio higher than 1:3 is counter-advised. In this case, with the use of a grid refinement ratio up to 1:3, a reduction of the total cell count by a factor up to 30.2 (compared to a conformal grid) can be achieved.

5. Limitations and future work

Although the study is based on a large number of LES simulations, it has a set of limitations that can give rise for future work:

- The standard Smagorinsky SGS model with $C_s = 0.1$ is used. Its performance has already been investigated for different flows [36,40,41]. Although a very good agreement between LES and experiments is shown, future studies should investigate different SGS models for LES of CHTC.
- Only forced convection is considered. Further research can include mixed convection.
- Although the comparison between LES on non-conformal and conformal grid is based on detailed analysis of the resolved quantities, future work should focus on further estimation of the numerical uncertainties that are introduced due to the use of non-conformal interfaces. Such estimation can be based on the pioneering work by Roache [42], Celik et al. [43], Oberkampf and Trucano [44] and others [45–47].
- The sensitivity analysis focuses on the impact of the computational grid resolution, subdomain size and grid refinement ratio. Future studies could focus on the impact of total number of subdomains.
- Future studies should consider evaluating the performance of non-conformal grids for the investigation of CHTC on inclined surfaces and configurations and on larger objects and ensembles that are representative of wider urban settings.
- The present study is intended to support future CFD studies of wind flow and heat transfer at surfaces of buildings or even blocks and districts in the urban environment. Despite the fact that this study shows the results of flow field and CHTC around a wall-mounted obstacle at Re number of 4440, which is too low for building applications, it should be noted that the main flow patterns presented here are similar to the flow patterns that appear around buildings. These flow patterns include impingement, the horseshoe vortex, roof and side separation bubble and von Karman vortex shedding in the wake. Given a sufficient resolution of the viscosity-affected region by the computational model, conclusions can be applied to flows at high Reynolds numbers as investigated in Refs. [7,8,24,48].

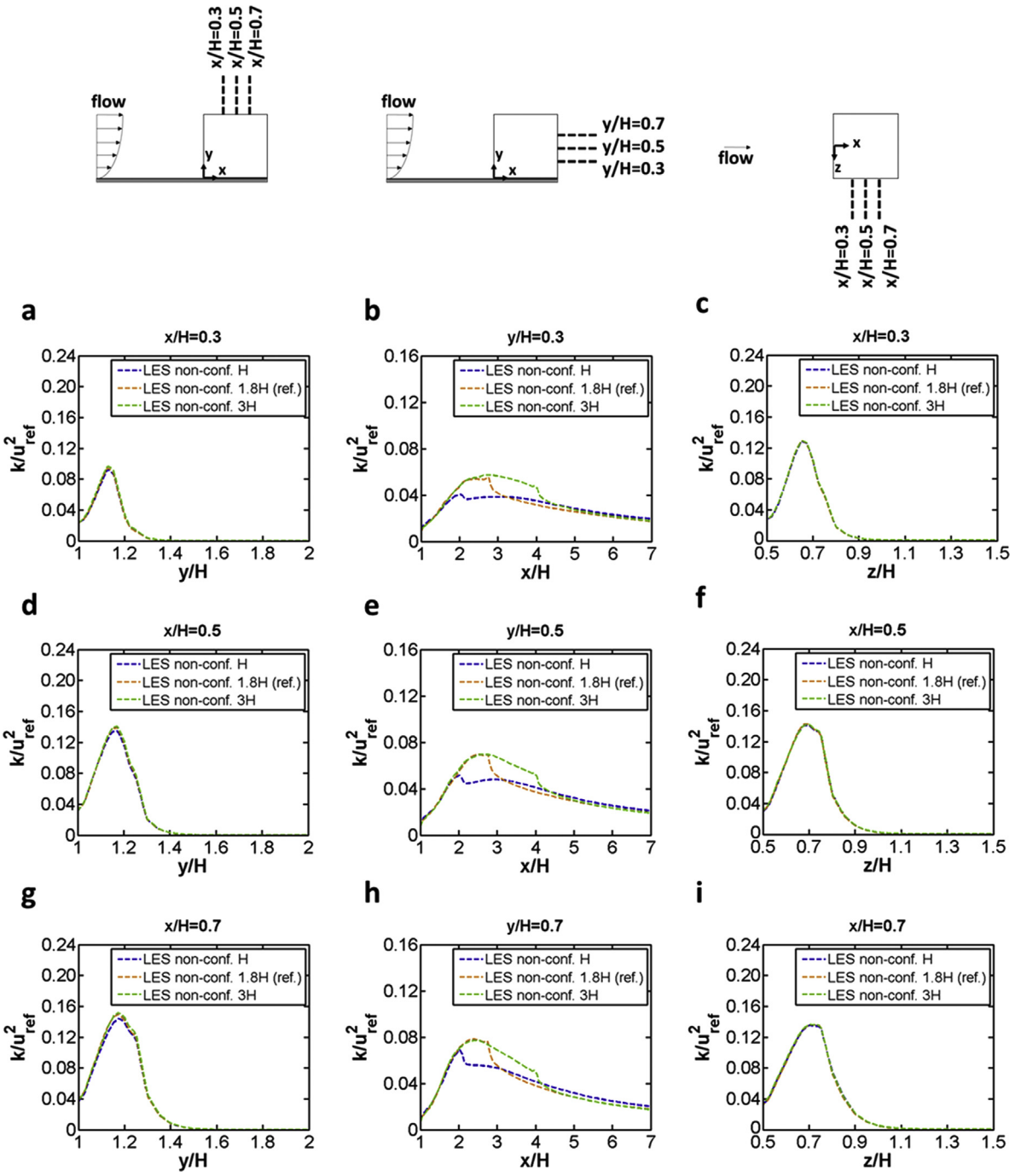

Fig. 16. The impact of subdomain size: CFD results of normalised turbulent kinetic along lines (a,d,g) at the top (plane z/H = 0), (b,e,h) in the wake (plane z/H = 0) and (c,f,i) at the side (plane y/H = 0.5) of the cube.

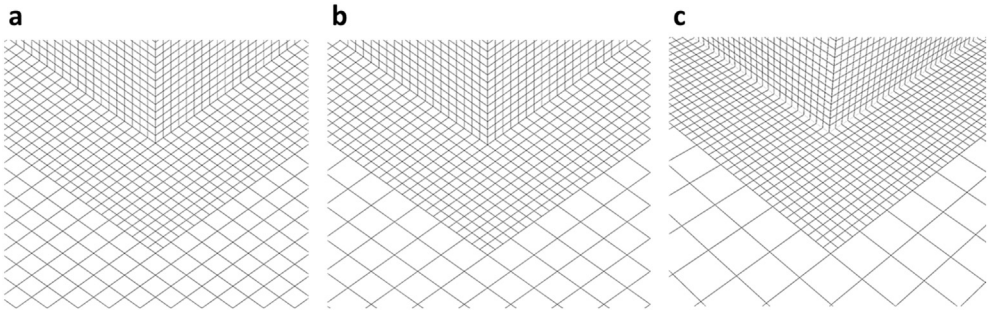

Fig. 17. Computational grids for grid refinement ratio analysis. Grid refinement ratio: (a) 1:2 (total number of cells: 1,404,653); (b) 1:3 (total number of cells: 320,526); (c) 1:4 (total number of cells: 206,416).

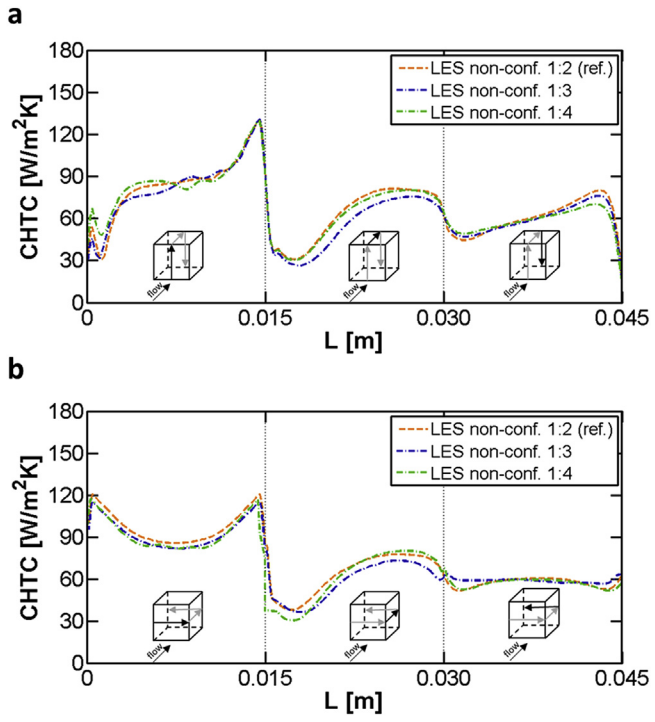

Fig. 18. The impact of grid refinement ratio: (a,b) CFD results of CHTC along lines on the cube surfaces.

6. Conclusions and recommendations

LES simulations of the flow field and forced convective heat transfer at the surfaces of a wall-mounted cubic obstacle are performed. The purpose is to evaluate the performance of non-conformal grids with cubic cells. The evaluation is performed in three steps. First, a comparison between LES on a non-conformal grid (40 cells per cube edge, 1.8H of subdomain size, 1:2 grid refinement ratio) and a conformal grid is carried out for normalised mean streamwise velocity, normalised Reynolds stresses and surface temperature. The results show a good agreement for the flow field (normalised mean streamwise velocity and normalised Reynolds stresses) and an average absolute difference for surface temperatures of about 0.9% (0.5 °C). In this case, the employment of a non-conformal grid results in a reduction of the total number of cells and CPU hours by a factor of 6.8 and 8.5, respectively. Second, results on the non-conformal grid are compared with wind-tunnel measurements and the agreement is quantified by validation metrics (FAC1.05, FAC1.3, NMSE and hit rate). Good average agreement is observed for the normalised mean streamwise velocity and normalised Reynolds stresses. As for surface temperature, average and maximum absolute deviation between simulated and experimental results are 2.0% (1.1 °C) and 7.6% (3.6 °C), respectively. In this case, for the validation metrics, FAC1.05 = 0.92 and NMSE = 0.0013. Third, a sensitivity analysis is conducted in which the influence of grid-related parameters (grid resolution, size of subdomain $\Omega_{nc,2}$ and grid refinement ratio) is evaluated. A set of conclusions and recommendations is made towards application of economic LES on non-conformal grids for wind flow and convective heat transfer around surface-mounted bluff bodies in turbulent boundary layer flow. These recommendations aim at reducing the total number of cells of the computational grids that employ non-conformal grids with cubic cells and very high near-wall grid resolution without significantly compromising accuracy. The grid sensitivity analysis shows that the grid resolution has a significant effect on the prediction of the flow field and CHTC. Although an increase of the grid resolution (here to 50 cells per cube edge) results in a decrease of the discontinuities in the profiles of normalised turbulent kinetic energy, an average deviation of 6.9% for CHTC is observed with the reference case (40 cells per cube edge). On the other hand, the analysis of the impact of the middle subdomain ($\Omega_{nc,2}$) size shows that only minor differences occur in the flow field and CHTC prediction. In this case, by varying the size to H and 3H, average absolute deviations of 2.2% and 1.1% are found for CHTC respectively, compared to the reference case (40 cells per cube edge, 1.8H of subdomain size, 1:2 grid refinement ratio). In addition, similar results for turbulent kinetic energy are observed. This recommends that, within the range investigated, the impact of middle subdomain size is negligible. Finally, the analysis of the impact of grid refinement ratio shows that the employment of a grid refinement ratio higher than 1:3 can result in significant local deviations of CHTC on the windward surface (up to 58.4%) and large discontinuities in the profiles of turbulent kinetic energy downstream of the bluff body compared to the reference case (40 cells per cube edge, 1.8H of subdomain size, 1:2 grid refinement ratio). By considering a non-conformal grid with grid refinement ratio 1:3 (40 cells per cube edge, 1.8H of subdomain size, 1:3 grid refinement ratio) between adjacent subdomains, average deviations of 6.4% for CHTC are observed. Considering the above, grid refinement ratios higher than 1:3 are counter-advised for the analysis of the flow field and CHTC around surface-mounted bluff bodies, like buildings. Following these recommendations, this study shows that non-conformal grids can strongly reduce the total cell count (here by a factor up to 30.2) compared to a conformal grid without significantly compromising the accuracy of results.

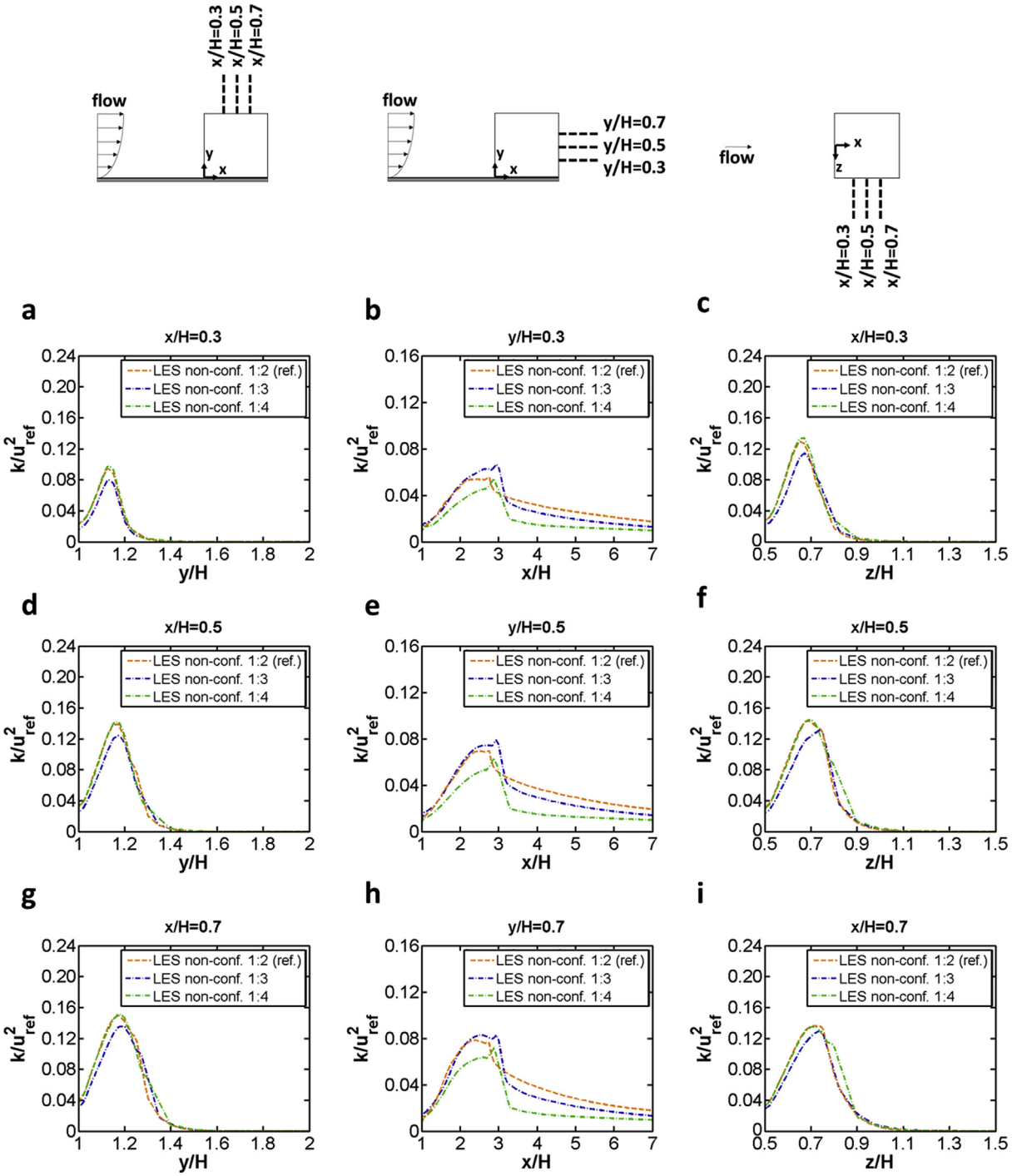

Fig. 19. The impact of grid refinement ratio: CFD results of normalised turbulent kinetic energy along lines (a,d,g) at the top (plane z/H = 0), (b,e,h) in the wake (plane z/H = 0) and (c,f,i) at the side (plane y/H = 0.5) of the cube.

Acknowledgements

The research is financially supported by the PhD Impulse Program of Eindhoven University of Technology in collaboration with the construction company Heijmans B.V., the Netherlands. Hamid Montazeri is currently a postdoctoral fellow of the Research Foundation - Flanders (FWO) and is grateful for its financial support (project FWO 12M5316N). The authors also gratefully acknowledge the partnership with ANSYS CFD.

References

[1] T. Stathopoulos, Computational wind engineering: past achievements and future challenges, J. Wind Eng. Ind. Aerodyn. 67–68 (1997) 509–532, http://dx.doi.org/10.1016/S0167-6105(97)00097-4.
[2] C.J. Baker, Wind engineering—past, present and future, J. Wind Eng. Ind. Aerodyn. 95 (2007) 843–870, http://dx.doi.org/10.1016/j.jweia.2007.01.011.
[3] B. Blocken, 50 years of computational wind engineering: past, present and future, J. Wind Eng. Ind. Aerodyn. 129 (2014) 69–102, http://dx.doi.org/10.1016/j.jweia.2014.03.008.
[4] J.A. Palyvos, A survey of wind convection coefficient correlations for building envelope energy systems' modeling, Appl. Therm. Eng. 28 (2008) 801–808, http://dx.doi.org/10.1016/j.applthermaleng.2007.12.005.
[5] B. Blocken, T. Stathopoulos, J. Carmeliet, J.L.M. Hensen, Application of computational fluid dynamics in building performance simulation for the outdoor environment: an overview, J. Build. Perform. Simul. 4 (2011) 157–184, http://dx.doi.org/10.1080/19401493.2010.513740.
[6] M. Mirsadeghi, D. Cóstola, B. Blocken, J.L.M. Hensen, Review of external convective heat transfer coefficient models in building energy simulation programs: implementation and uncertainty, Appl. Therm. Eng. 56 (2013) 134–151, http://dx.doi.org/10.1016/j.applthermaleng.2013.03.003.
[7] B. Blocken, T. Defraeye, D. Derome, J. Carmeliet, High-resolution CFD simulations for forced convective heat transfer coefficients at the facade of a low-rise building, Build. Environ. 44 (2009) 2396–2412, http://dx.doi.org/10.1016/j.buildenv.2009.04.004.
[8] J. Liu, J. Srebric, N. Yu, Numerical simulation of convective heat transfer coefficients at the external surfaces of building arrays immersed in a turbulent boundary layer, Int. J. Heat. Mass Transf. 61 (2013) 209–225, http://dx.doi.org/10.1016/j.ijheatmasstransfer.2013.02.005.
[9] S. Murakami, Comparison of various turbulence models applied to a bluff body, J. Wind Eng. Ind. Aerodyn. 46–47 (1993) 21–36, http://dx.doi.org/10.1016/0167-6105(93)90112-2.
[10] W. Rodi, Comparison of LES and RANS calculations of the flow around bluff bodies, J. Wind Eng. Ind. Aerodyn. 69–71 (1997) 55–75, http://dx.doi.org/10.1016/S0167-6105(97)00147-5.
[11] K.B. Shah, J.H. Ferziger, A fluid mechanicians view of wind engineering: large eddy simulation of flow past a cubic obstacle, J. Wind Eng. Ind. Aerodyn. 67–68 (1997) 211–224, http://dx.doi.org/10.1016/S0167-6105(97)00074-3.
[12] Y. Tominaga, A. Mochida, S. Murakami, S. Sawaki, Comparison of various revised k–ε models and LES applied to flow around a high-rise building model with 1:1:2 shape placed within the surface boundary layer, J. Wind Eng. Ind. Aerodyn. 96 (2008) 389–411, http://dx.doi.org/10.1016/j.jweia.2008.01.004.
[13] P.P. Sullivan, J.C. McWilliams, C.-H. Moeng, A grid nesting method for large-eddy simulation of planetary boundary-layer flows, Bound.-Layer Meteorol. 80 (1996) 167–202, http://dx.doi.org/10.1007/BF00119016.
[14] B. Boersma, M. Kooper, F. Nieuwstadt, P. Wesseling, Local grid refinement in large-eddy simulations, J. Eng. Math. 32 (1997) 161–175.
[15] U. Piomelli, S. Kang, F. Ham, G. Iaccarino, Effect of discontinuous filter width in large-eddy simulations of plane channel flow, in: Proc. Summer Progr, 2006, Center for Turbulence Research, 2006, pp. 151–162.
[16] M. Vanella, U. Piomelli, E. Balaras, Effect of grid discontinuities on large-eddy simulation statistics and flow fields, J. Turbul. 9 (2008) 37–41, http://dx.doi.org/10.1080/14685240802446737.
[17] E.R. Meinders, Experimental Study of Heat Transfer in Turbulent Flows over Wall-mounted Cubes, Technische Universiteit Delft, 1998.
[18] E.R. Meinders, K. Hanjalic, R.J. Martinuzzi, Experimental study of the local convection heat transfer from a wall-mounted cube in turbulent channel flow, J. Heat. Trans. - T. ASME 121 (1999) 564–573, http://dx.doi.org/10.1115/1.2826017.
[19] G.M. Carlomagno, L. De Luca, Infrared thermography in heat transfer, in: W.J. Yang (Ed.), Handbook of flow visualisation, Taylor & Francis, 1989, pp. 531–553.
[20] J. Franke, A. Hellsten, H. Schlünzen, B. Carissimo, Best practice guideline for the CFD simulation of flows in the urban environment, Cost Action 732 (2007).
[21] Y. Tominaga, A. Mochida, R. Yoshie, H. Kataoka, T. Nozu, M. Yoshikawa, T. Shirasawa, AIJ guidelines for practical applications of CFD to pedestrian wind environment around buildings, J. Wind Eng. Ind. Aerodyn. 96 (2008) 1749–1761, http://dx.doi.org/10.1016/j.jweia.2008.02.058.
[22] B. Blocken, Computational Fluid Dynamics for urban physics: importance, scales, possibilities, limitations and ten tips and tricks towards accurate and reliable simulations, Build. Environ. 91 (2015) 219–245, http://dx.doi.org/10.1016/j.buildenv.2015.02.015.
[23] B. Blocken, T. Stathopoulos, J. Carmeliet, CFD simulation of the atmospheric boundary layer – wall function problems, Atmos. Environ. 41 (2007) 238–252, http://dx.doi.org/10.1016/j.atmosenv.2006.08.019.
[24] H. Montazeri, B. Blocken, D. Derome, J. Carmeliet, J.L.M. Hensen, CFD analysis of forced convective heat transfer coefficients at windward building facades: influence of building geometry, J. Wind Eng. Ind. Aerodyn. 146 (2015) 102–116, http://dx.doi.org/10.1016/j.jweia.2015.07.007.
[25] R.W. Fox, A.T. McDonald, P.J. Pritchard, Introduction to Fluid Mechanics, second ed., John Wiley & Sons, New York, 1998.
[26] A. Smirnov, S. Shi, I. Celik, Random flow generation technique for Large Eddy Simulations and particle-dynamics modeling, J. Fluids Eng. 123 (2001) 359–371, http://dx.doi.org/10.1115/1.1369598.
[27] ANSYS, Fluent, Release 15.0, Theory Guide, ANSYS Inc, 2013.
[28] T.-H. Shih, W.W. Liou, A. Shabbir, Z. Yang, J. Zhu, A new k-ε eddy viscosity model for high Reynolds number turbulent flows, Comput. Fluids 24 (1995) 227–238, http://dx.doi.org/10.1016/0045-7930(94)00032-T.
[29] M. Wolfshtein, The velocity and temperature distribution in one-dimensional flow with turbulence augmentation and pressure gradient, Int. J. Heat. Mass Transf. 12 (1969) 301–318, http://dx.doi.org/10.1016/0017-9310(69)90012-X.
[30] J. Smagorinsky, General circulation experiments with the primitive equations, Mon. Weather Rev. 91 (1963) 99–164.
[31] J. Kim, P. Moin, Application of a fractional-step method to incompressible Navier-Stokes equations, J. Comput. Phys. 59 (1985) 308–323, http://dx.doi.org/10.1016/0021-9991(85)90148-2.
[32] J.B. Bell, P. Colella, H.M. Glaz, A second-order projection method for the incompressible Navier-Stokes equations, J. Comput. Phys. 85 (1989) 257–283, http://dx.doi.org/10.1016/0021-9991(89)90151-4.
[33] S. Armfield, R. Street, The fractional-step method for the Navier-Stokes equations on staggered grids: the accuracy of three variations, J. Comput. Phys. 153 (1999) 660–665, http://dx.doi.org/10.1006/jcph.1999.6275.
[34] J.K. Dukowicz, A.S. Dvinsky, Approximate factorization as a high order splitting for the implicit incompressible flow equations, J. Comput. Phys. 102 (1992) 336–347, http://dx.doi.org/10.1016/0021-9991(92)90376-A.
[35] J. Perot, An analysis of the fractional step method, J. Comput. Phys. 108 (1993) 51–58, http://dx.doi.org/10.1006/jcph.1993.1162.
[36] P. Gousseau, B. Blocken, G.J.F. van Heijst, Quality assessment of Large-Eddy Simulation of wind flow around a high-rise building: validation and solution verification, Comput. Fluids 79 (2013) 120–133, http://dx.doi.org/10.1016/j.compfluid.2013.03.006.
[37] M. Schatzmann, H. Olesen, J. Franke, COST 732 model evaluation case studies: approach and results, Cost Action (2010).
[38] VDI, VDI Guideline 3783, Part 9, Environmental Meteorology - Prognostic Microscale Wind Field Models - Evaluation for Flow Around Buildings and Obstacles, Commission of Air Pollution Prevention of VDI and DIN, 2005. Düsseldorf, Germany.
[39] I.B. Celik, Z.N. Cehreli, I. Yavuz, Index of resolution quality for large eddy simulations, J. Fluids Eng. Trans. ASME 127 (2005) 949–958, http://dx.doi.org/10.1115/1.1990201.
[40] S. Krajnovic, L. Davidson, Large-eddy simulation of the flow around a bluff body, AIAA J. 40 (2002) 927–936, http://dx.doi.org/10.2514/3.15142.
[41] M. Popovac, Modelling and Simulation of Turbulence and Heat Transfer in Wall-bounded Flows, Technische Universiteit Delft, 2006.
[42] P.J. Roache, Verification and Validation in Computational Science and Engineering, Hermosa Publishers, 1998.
[43] I.B. Celik, U. Ghia, P.J. Roache, C.J. Freitas, H. Coleman, P.E. Raad, Procedure for estimation and reporting of uncertainty due to discretization in CFD applications, J. Fluids Eng. 130 (2008) 78001, http://dx.doi.org/10.1115/1.2960953.
[44] W.L. Oberkampf, T.G. Trucano, Verification and validation in computational fluid dynamics, Prog. Aerosp. Sci. 38 (2002) 209–272, http://dx.doi.org/10.1016/S0376-0421(02)00005-2.
[45] F. Stern, R.V. Wilson, H.W. Coleman, E.G. Paterson, Comprehensive approach to verification and validation of CFD simulations—part 2: application for RANS simulation of a cargo/container ship, J. Fluids Eng. 123 (2001) 793, http://dx.doi.org/10.1115/1.1412235.
[46] L. Eça, M. Hoekstra, A procedure for the estimation of the numerical uncertainty of CFD calculations based on grid refinement studies, J. Comput. Phys. 262 (2014) 104–130, http://dx.doi.org/10.1016/j.jcp.2014.01.006.
[47] AIAA, Guide for the Verification and Validation of Computational Fluid Dynamics Simulations (AIAA G-077-1998(2002)), 1998, http://dx.doi.org/10.2514/4.472855.001.
[48] T. Defraeye, B. Blocken, J. Carmeliet, CFD analysis of convective heat transfer at the surfaces of a cube immersed in a turbulent boundary layer, Int. J. Heat. Mass Transf. 53 (2010) 297–308, http://dx.doi.org/10.1016/j.ijheatmasstransfer.2009.09.029.